Size-dependence of surface-rooted three-dimensional convective objects in continental shallow cumulus simulations

P. J. Griewank [1,3], T. Heus [2], R. A. J. Neggers, [1]

[1]University of Cologne, Germany
[2]Cleveland State University, Ohio, USA
[3]University of Vienna, Austria

Key Points:

- A 3D clustering analysis is applied to large-eddy simulations of shallow cumulus cloud fields as observed at the ARM SGP site
- Plume-like surface-rooted coherent convective clusters are omnipresent, with cluster depth being strongly dependent on diameter
- Substantial size- and height dependence is also found in profiles of cluster geometric, thermodynamic, kinematic and flux properties

Corresponding author: P. J. Griewank, philipp.griewank@univie.ac.at

Abstract

A clustering method is applied to high resolution simulations of shallow continental convection to investigate the size dependence of coherent structures in the convective boundary layer. The study analyses the geometry of the clusters, along with their profiles of vertical velocity and total water. The main science goal is to assess various assumptions often used in spectral mass-flux convection schemes. Novel aspects of the study methodology include i) a newly developed clustering algorithm, and ii) an unprecedentedly large number of simulations being analysed. In total 26 days of LASSO simulations at the ARM-SGP site are analyzed, yielding roughly one million individual clusters. Plume-like surface-rooted coherent convective clusters are found to be omnipresent, the depth of which is strongly dependent on cluster size. The largest clusters carry vertical structures that are roughly consistent with the classic buoyancy-driven rising plume model, while smaller clusters feature considerable variation in top height. The cluster area is found to strongly vary with height and size, with small clusters losing mass and large clusters gaining mass below cloud base. Similar size dependence is detected in kinematic and thermodynamic properties, being strongest above cloud base but much weaker below. Finally the efficiency of the top-hat approach in flux parameterization is investigated, found to be 80-85 % including a weak but well-defined dependence on cluster size. Implications of the results for spectral convection scheme development are briefly discussed.

Plain Language Summary

This paper studies updrafts, which are volumes of warm air travelling upwards in the atmosphere, using high-resolution simulations. These simulations have sufficient resolution to capture how air warmed at the surface by the sun travels upwards. These updrafts are responsible for the formation of cumulus clouds. What separates this study from others is the newly developed method used to detect these updrafts in the model output, and the comparatively large amount of simulations analysed. The model domain is large enough to contain thousands of updrafts at any time throughout the day. 26 days of simulations over the great plains in Oklahoma are used, yielding about a million simulated updrafts in total for us to study. From our results we conclude that there is a clear positive relationship between updraft width and height. Thinner updrafts seldom reach up to the cloud base, and they tend to get thinner the further away they are from the surface. In contrast, we find that the larger updrafts are wider at cloud base than at the

surface. Other aspects of the updrafts, such as their vertical velocity and moisture transport, are studied to determine how these properties vary with the width of the updrafts.

1 Introduction

Meteorologists have attempted to represent unresolved surface driven convection in atmospheric models since the very beginning of computational atmospheric modelling. While many methods have been developed and applied successfully, shortcomings in convective parametrizations still cause uncertainty among numerical climate simulations (Sherwood et al., 2014; Vial et al., 2016), as well as biases in the onset of continental precipitation in numerical weather prediction (Grabowski et al., 2006). The most popular and widespread class of convective parametrizations use the mass-flux approach, which was developed decades ago (Yanai et al., 1973; Arakawa & Schubert, 1974) and is still an active field of research and development (e.g. Lopez-Gomez et al., 2020; Cohen et al., 2020). What all mass-flux approaches have in common is that they rely on one or more advective plumes to vertically transport near-surface air to higher levels, experiencing lateral mixing on the way.

Mass flux schemes can roughly be divided into single and multi-plume approaches. Single-plume approaches typically follow the "bulk" paradigm, in that all unresolved convective objects in a gridbox are represented through a single parametrized plume (e.g. Yanai et al., 1973; Sakradzija et al., 2015; Tan et al., 2018). In contrast, multi-plume approaches make use of a spectrum of plumes to achieve the same goal, thus maintaining extra information in the dimension in which the spectrum is defined (e.g. Arakawa & Schubert, 1974; Neggers, 2015; Suselj et al., 2019; Baba, 2020). A special subclass of spectral mass flux approaches are those formulated in size space, thus assuming dependence on the width of the transporting objects. Recent research has shown that size-dependent spectral approaches can in principle capture population-internal interactions between plumes (Neggers, 2015), gray-zone scaling (Brast et al., 2018), convective stochasticity (Sakradzija & Klocke, 2018) and deep convective memory (Hagos et al., 2018). Some size-dependent spectral approaches have successfully been implemented in operational weather forecasting (Olson et al., 2019).

With size dependence being at the foundation of many mass flux approaches, it is essential to obtain observational evidence for the existence of this dependence in nature.

Size dependence has indeed been observed in cumulus cloud populations, but this has for a long time mostly been limited to size distributions of object number, often based on vertical projections (Plank, 1969; Benner & Curry, 1998; Wood & Field, 2011). It has proven much harder to establish clear size dependence in plume internal properties such as thermodynamic state, vertical velocity and associated transport, including their vertical structure. The main problem is that current instrumentation can not yet capture the full 3D structure of convective objects at a sufficient temporal and spatial resolution. Targeted observations commonly only sample a subset of relevant variables from a limited number of convective objects, with sample sizes too small to draw any meaningful conclusions about general applicability. Recent observational studies have slowly started to fill this data gap, using continuously operating instruments at permanent meteorological sites (e.g. Ghate et al., 2011; Kleiss et al., 2018; Romps & Öktem, 2018; Zheng et al., 2021). A few recent studies used multiple years worth of vertically pointing remote sensing data at the Atmospheric Radiation Measurement Southern Great Plains site (ARM-SGP) to investigate size dependence. Lamer and Kollias (2015), Lareau et al. (2018) and Lareau (2020) inferred from chord-length analyses that continental shallow clouds do indeed have a clear size dependence in their vertical velocity and specific humidity. Despite this clear progress, observational data on the vertical structure of plume properties and the associated size dependence is still pending.

A virtual alternative for investigating the size dependence in moist convection is provided by high resolution simulations of turbulence and convection, also know as Large Eddy Simulation (LES). Convective processes can be considered for the largest part resolved in these numerical realizations, which can be closely constrained by observations of the atmospheric state on days and at sites of interest (Neggers et al., 2012; van Laar et al., 2019; Gustafson et al., 2020). Indeed a considerable number of LES studies on the shape of individual clouds and their size dependence have been conducted (e.g. Neggers et al., 2003; Heus & Seifert, 2013). Neggers (2015) reported size dependence in cloud-average profiles of thermodynamic and kinematic state for subtropical marine cumulus cloud fields. Recent studies of deep convection have reported similar links between the width of convective objects, their entrainment, and their resulting height and strength (Peters, Nowotarski, & Mullendore, 2020; Peters, Morrison, et al., 2020). In an effort to bridge the gap between observations and high resolution simulations, Griewank et al. (2020) applied the same data analysis strategy in LES that Lareau et al. (2018) applied to ob-

servations. They found that the simulations they analysed successfully reproduced the observed sub-cloud circulations, and provided further evidence that the properties of continental shallow cumulus clouds vary with size.

In this study we use a library of LES realizations of continental shallow cumulus at the ARM-SGP site to investigate the size dependence in the properties of resolved individual convective objects. The properties we focus on are the vertical profiles of object area, vertical velocity, and total water mixing ratio, which are all needed for spectral mass flux parameterizations of surface driven convection. To achieve these goals we develop a tailor-made object clustering method. This method is inspired by previously proposed algorithms to seamlessly track convective motions across cloud base (Couvreux et al., 2009; Efstathiou et al., 2020; Denby et al., 2020), but also differs in some key aspects. Another novelty of our study is the type and number of LES runs that are analysed. While most previous work is based on the analysis of a single case (e.g. Couvreux et al., 2009), which is most often a quasi-steady maritime case (e.g. Heus et al., 2009; Neggers, 2015; Park et al., 2018), we analyse simulations of 26 independent days of summertime shallow convection at the ARM-SGP site, as part of the LASSO initiative (Gustafson et al., 2020). These exact runs were also used in the recent study by Griewank et al. (2020), and have been extensively evaluated against lidar observations of vertical velocity and water vapor.

The data and the clustering method used in this study are described in detail in Section 2. The sensitivity of the clustering approach to is assessed in Section 3, yielding a setting that is subsequently used to investigate size dependence in cluster properties in Section 4. Our main results and conclusions are summarized and discussed in Section 5.

2 Data and Methods

2.1 Data

2.1.1 Cases

For the current study we selected 26 days with shallow cumulus convection over the Department of Energy's Atmospheric Radiation Measurement site in the Southern Great Plains (ARM-SGP). These days are all part of the Large-Eddy Simulation (LES) ARM Symbiotic Simulation and Observation (LASSO; Gustafson et al., 2017, 2020) database.

These realistic and routine simulations of cumulus fields over the ARM-Southern Great Plains (SGP) observatory in Oklahoma were run using a variety of initial conditions and model settings. For each day in the list in Table 1, we selected the setting yielding the best match to the observations in cloud cover and liquid water path, according to the LASSO Bundle Browser (`https://adc.arm.gov/lassobrowser`) (skill scores above 0.3).

2.1.2 Model setup

For all 26 cases LES runs were generated with the MicroHH code (van Heerwaarden et al., 2017). This Large Eddy Simulation model has been validated against a wide range of standard cases, including shallow cumulus intercomparsion cases in marine (e.g. BOMEX Siebesma et al., 2003) and continental (e.g. ARM, Brown et al., 2002) conditions.

The experimental setup includes a simulated domain with horizontal and vertical dimensions of 25.6 x 25.6 km^2 and 9 km, respectively. Below 6 km a 25 m grid spacing is used in all directions, a resolution 4x higher compared to the standard LES runs in the LASSO archive. Estimating that the smallest resolvable feature is about four times larger than the grid size, the 25 m grid spacing should allow reliable simulation of plumes with sizes down to 100 m. Above 6 km height the vertical gridspacing stretches from 25 m to 150 m. Adaptive time stepping with a constant Courant-Friedrichs-Lewy criterion resulted in an effective time discretization between 1 and 2 seconds. Periodic boundary conditions were adopted, as were homogeneous and prescribed surface fluxes, as well as a prescribed profile of radiative tendencies. MicroHH uses a double moment warm microphysics scheme, with a fixed cloud droplet number concentration of 200 cm^{-3}.

During the runs, instantaneous three-dimensional snapshots of all thermodynamic variables were saved every 1800 s. To trace the behavior of the plumes, a passive scalar c was included as a prognostic variable in the runs, largely following the methodology of Couvreux et al. (2009). This scalar is emitted with a fixed, homogeneous, surface flux, and removed from the domain by an exponential decay with a half life time of 1800 s. The scalar concentration is only used in relative amounts, rendering the actual amount of the surface flux irrelevant and set to $1 \cdot 10^{-5}$ kg m^{-2} s^{-1}.

Note that the 26 runs used in this study are a subset of the 28 runs which Griewank et al. (2020) evaluated against observations of vertical velocity, water vapor, and cloud

Table 1. Dates of simulations included in the analysis (in Month/Day).

2015	06/06	06/09	06/27		
2016	05/18	05/30	06/11	06/19	06/25
	07/19	07/20	08/18	08/19	08/30
2017	05/09	06/05	06/27	07/04	07/16
	07/19	07/20	07/22		
2018	05/22	06/06	07/05	07/09	07/10

fraction. The 2 days not included were rejected due to technical errors that occurred in regards to the passive tracer used for clustering. Crucial for this paper is that Griewank et al. (2020) showed that the runs reproduce both the shape and amplitude of the observed sub-cloud vertical velocity fields, as well as the observed relationship between cloud chord length and updraft strength.

While the bulk of the statistical analysis in this study relies on all 26 cases, we selected a single day to illustrate the working of the cluster algorithm and its sensitivities (see Section 3). As can be seen from the true color MODIS (MODerate-resolution Imaging Spectroradiometer) satellite image shown in Figure 1, on this day more or less homogeneous shallow cumulus cloud fields are present over most of western Oklahoma. Deeper convection with cold pools occur farther to the south along the border to Texas. To give an idea of the simulated clouds we also included a 3D render of the model clouds at noon, positioned above a cloud free MODIS image of the surface (Figure 2). The smallest white dots in the satellite picture correspond to clusters of individual clouds in the model runs (Figure 2). There is no unique feature about this day that made us choose it as our illustrative example, our only selection requirement was that the run should reach a cloud fraction above 10 % during the day (see Figure 2 of (Griewank et al., 2020)).

2.2 Clustering algorithm

Many clustering methods have been developed over the last decades to investigate various aspects of convection, but none suited to our task. We adopt a new method to meet the following four requirements necessary to address our research questions:

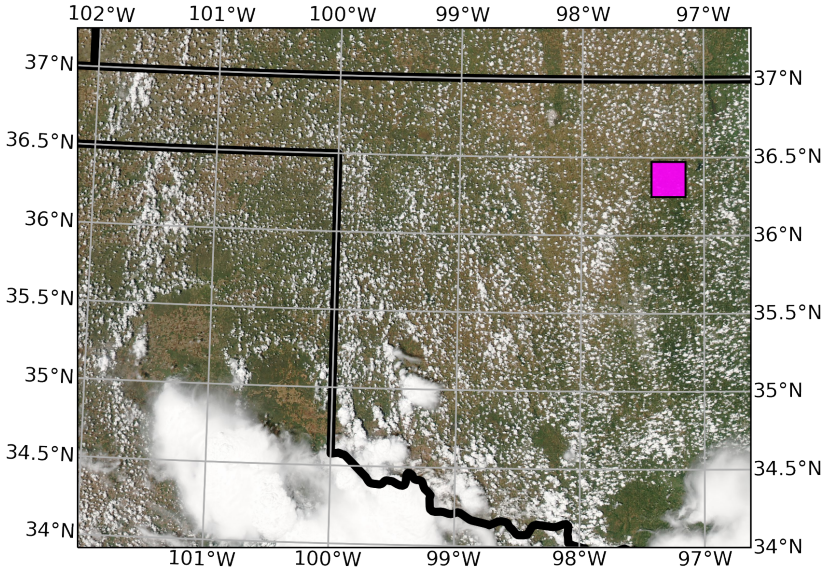

Figure 1. MODIS Aqua true color image of a convective cloud field over western Oklahoma, USA, in the early afternoon of 11 June 2016. Image data obtained at 250 m resolution through NASA Worldview. The state borders are marked in black, and the magenta box marks the size and location of the model domain described in Subsection 2.1 and shown in Figure 2.

Figure 2. 3D rendering of simulated clouds over the ARM SGP site during the 11 June 2016 LASSO case. The 3D rendering is performed using Blender (http://blender.org), with the ray tracing acting on cloud liquid water. A MODIS cloud free satellite image is used as the surface, the MODIS image from the same day is shown in Figure 1.

1. Coherent clusters must be identified in three dimensional space, labeled individually, and sorted by size;
2. Individual clusters can be directly adjacent to each other;
3. Clusters must able to extend from the surface up till cloud top, and be definable also in absence of condensate;
4. The method must be robust and computationally efficient enough to be generally applicable to multiple cases.

The first requirement disqualifies many previously published approaches which only distinguish between convective and non-convective air, and do not consider the size and shape of individual convective objects (e.g. Siebesma et al., 2007; Couvreux et al., 2009; Chinita et al., 2018; Efstathiou et al., 2020). The second requirement is designed to prevent clusters potentially taking a dendritic, elongated shape covering the whole domain. This requirement means that individual clusters can not solely be defined by their spatial connectivity, as done for example by Brient et al. (2019). The third requirement eliminates approaches relying on cloud properties to define clusters (e.g Neggers, 2015; Park et al., 2018; Tan et al., 2018; Suselj et al., 2019). The fourth requirement rules out computationally demanding methods such as Lagrangian particle or object tracking through time (e.g. Romps & Kuang, 2010; Dawe & Austin, 2012; Heus & Seifert, 2013; Hernandez-Deckers & Sherwood, 2016), or 3D filtering of the flow-field (Park et al., 2016).

The clustering method recently proposed by Denby et al. (2020) in principle fulfills these four requirements. While it inspires the method adopted here, some key differences also exist, as explained below. Similar to previous methods a passive tracer C is required, being released at the surface and decaying over time. This easy to implement and computationally cheap approach was initially proposed by (Couvreux et al., 2009), and has become widely used. A high tracer concentration at a specific height level shows that this air was in contact with the surface more recently than the surrounding air, and the higher the concentration the quicker the air travelled upward and the less mixing it experienced along the way. Our method consists of **four steps**, as explained below. An idealized 2D example (see Figure 3) and an actual 2D slice through a 3D snapshot (see Figure 4) are used to illustrate key concepts.

2.2.1 Step 0: Anomaly normalization

Before we begin our clustering approach we first convert the tracer concentration $C(x, y, z)$ of each snapshot to a horizontal tracer anomaly, which we normalize by the standard deviation of the tracer at each height ($\sigma_C(z)$).

$$c'(x, y, z) = \frac{C(x, y, z) - \overline{C}(z)}{\sigma_C(z)} \tag{1}$$

where c' stands for the normalized anomaly, the overbar for the horizontal mean, and σ for the standard deviation. An example of the normalized tracer anomaly at a specific height is shown in Figure 4 a. To avoid spurious tracer anomalies in regions where the total tracer concentration is so small that numerical noise affects the results, the horizontally mean tracer concentration $\overline{C}(z)$ is set to $1 \cdot 10^{-10}$ at heights where the mean concentration value is lower.

2.2.2 Step 1: Decomposition

Our clustering algorithm first separates the 3D model snapshot into 3 distinct areas. Following Couvreux et al. (2009), we first separate the whole domain into a ***convective*** and ***non-convective*** area. All cells which have a tracer anomaly c' higher than a threshold value m_{mask} are part of the convective area, all others are masked out and considered non-convective. The third area is a subsection of the convective area, which we call the ***core*** area. It consists of all cells with a tracer anomaly surpassing a higher threshold m_{core}, which must be larger than m_{mask}. In Section 3 we will look into how the threshold values chosen affect the resulting clustering. In our simplified 2D example shown in Figure 3, the grey pixels in Subplot a are the non-convective pixels, the light blue pixels are the convective pixels, and the dark red pixels are the cells which belong to the core area. Figure 4 b shows what the convective and core areas would be for a range of threshold values used.

Note that Couvreux et al. (2009) also used vertical velocity and cloud water to determine which regions are convective, but we only use the tracer concentration, in line with the recent approaches of Brient et al. (2019); Efstathiou et al. (2020), and Denby et al. (2020).

2.2.3 Step 2: Cores and watershedding

We now define individual cluster cores from all cells in the core area. We do this by treating all cells which are directly connected to each other as one core, with connectivity being defined as a neighboring cell in x, y, or z direction (no diagonals). So for the 2D example shown in Figure 3 a, there are a total of 6 core cells, which form 4 individual cluster cores. In 3D the connectivity can be much more convoluted.

Starting at the individual cores, the surrounding convective area is then scanned outwards and labeled until it is completely filled. This is done using a watershedding algorithm, and the speed of the outward scan in 3D space is determined by the gradient of $c'(x, y, z)$. This is illustrated in Figure 3 b, where the 4 cores have spread out to fill all the convective regions shown in light blue in Subfigure 3 a.

A convective area which contains no core will not be included in a cluster, and will at the end be reverted back to the non-convective area (see the 4 pixels in the bottom left of Figure 3). Watershedding is used in a similar manner in the clustering method of Denby et al. (2020), which in turn is heavily inspired by that of Park et al. (2018). The key difference is that the initial points of their watersheds are local maxima in the tracer anomaly, and not the connected cores we use.

In the non idealized example shown in Figure 4, we chose a slice that contains two large plumes with diffuse borders and tracer anomalies between 1 and 3 standard deviations, as well as various smaller more compact plumes with higher tracer anomalies. The two subfigures on the right of Figure 4 show the resulting clusters for two different core thresholds. While the more compact plumes (e.g. at x=1 km,y=1 km and x=6 km, y=4 km) remain a single cluster, the larger plumes separate into multiple individual clusters. But a higher core threshold does not automatically mean that more individual clusters are formed. For example, the small group of clusters at x=1 km and y=4km shows the opposite behaviour (Figure 4 c,d).

2.2.4 Step 3: Merging and cleaning

The aim of the final step of the clustering is to reduce the large amount of very small but numerous clusters, many which are direct neighbors of much larger clusters. We do this primarily for practical reasons, as these small but numerous clusters substantially

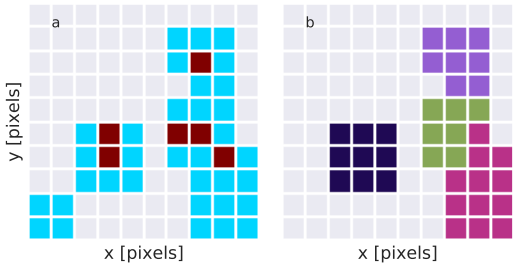

Figure 3. Simplified illustration of the clustering algorithm described in Subsection 2.2 in 2D. Light blue convective cells and core cells (a), and resulting clusters each marked by a random color (b).

increase the memory footprint and computation time of the post-processing, while contributing very little to the total volume or fluxes. We reduce the clusters in two ways. Firstly, by merging a small cluster to a larger neighboring cluster if they are directly in contact with each other and the ratio in volume between the clusters exceeds a certain threshold. We choose a value of 100 for this threshold to ensure that clusters are only merged when the larger is at least two orders of magnitude larger. Neighbors are merged iteratively, starting from the largest clusters down to the smallest. This process is repeated until no more mergeable neighbors remain. And at the very end we remove all clusters that have less than 30 cells. Brient et al. (2019) also use such a minimum cluster size, although their default value of 1000 cells is substantially larger than ours. It should be noted that while our clustering approach itself does not filter out many clusters, we will often only analyse a subset of all clusters (Section 4).

3 Clustering sensitivity

In this section we assess how the clustering algorithm reacts to changes to the two main free parameters of our clustering algorithm, namely the threshold values that determine what counts as convective and what counts as core-convective. We will not look into the effect of the tracer decay time, as both Park et al. (2016) and Brient et al. (2019) have already shown that the effect is negligible for decay times between 15 and 60 minutes, for similar shallow convection cases. For simplicity's sake we will illustrate the effects using a single snapshot from the 2016-06-11 case, at a local time of 13:30 when convection is approximately at its most intense (profiles of total water, potential temperature, and cloud fraction are shown in Figure 5 a and e). The basic clustering behaviour

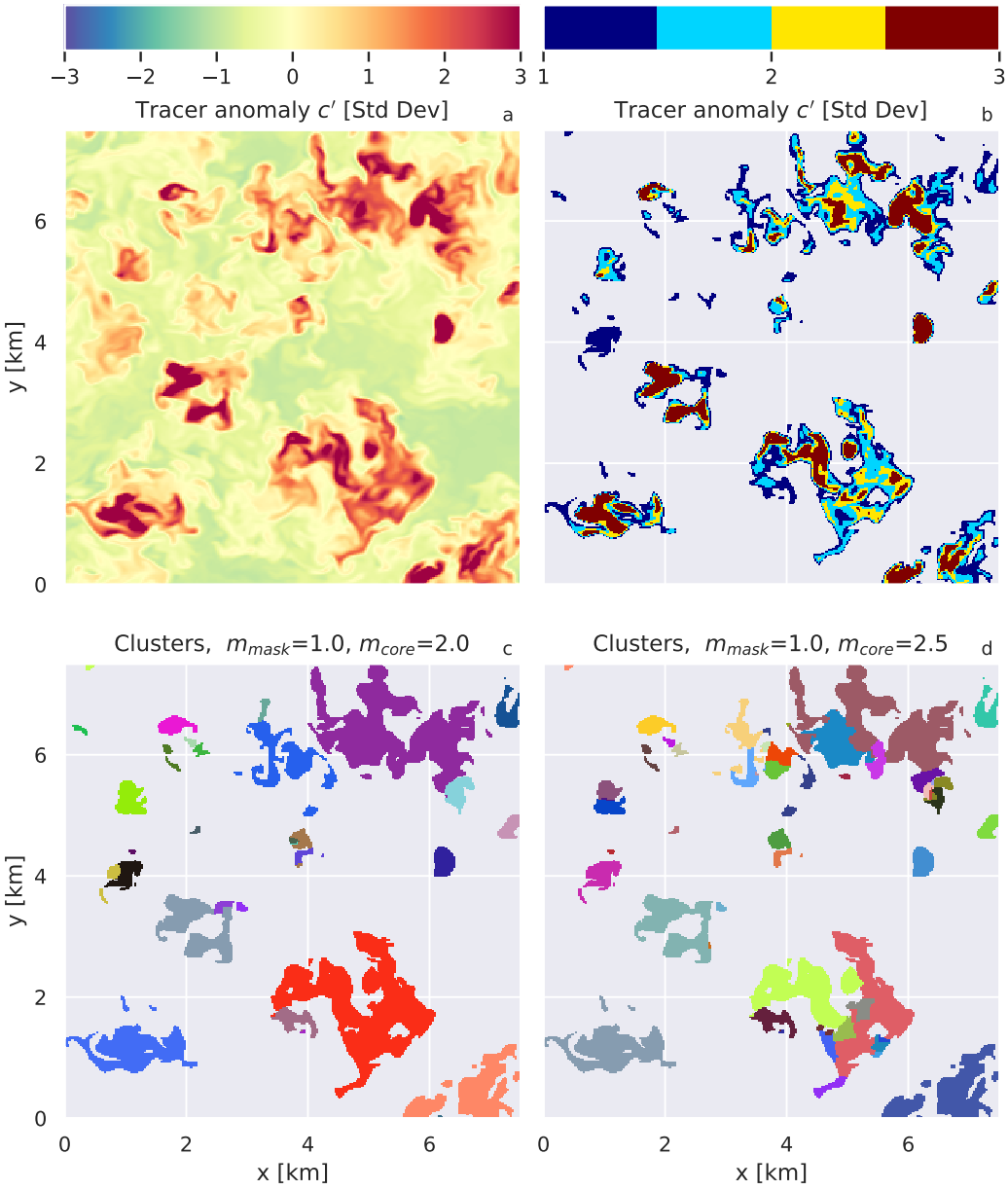

Figure 4. Surface emitted tracer anomaly regularized by standard deviation at 1500 m height at 13:30 local time, 2016-06-11 (top). Only a 7x7 km subdomain of the full 25x25 km model domain is shown. The same data is plotted with a smooth (left) and discrete color map of the threshold values used in Subsection 3 (right). Clusters resulting from different core thresholds are represented by a randomized color (bottom).

is consistent across snapshots. We will first only look at the properties of the total convective area, before we address how the total convective area is decomposed into individual clusters of varying size.

3.1 Total convective area

In this subsection we look at the properties over the total convective area, defined as the region with a tracer anomaly greater than m_{mask}, for $m_{mask} \in \{1.0, 1.5, 2.0\}$ (in units of standard deviation). Our goal here is to ensure that using the surface emitted tracer C to mask out the convective regions works as expected from previous research. And indeed, the profiles of the convective volume (Figure 5 b) closely mirror those of other studies. No matter which threshold is used, the area is relatively constant with height until cloud base, but decreases above cloud base with a small peak at the inversion height. Using a threshold of 1 results in roughly 15 % of the domain below cloud base being classified as convective, which is quite similar to the values reached by Couvreux et al. (2009) and Efstathiou et al. (2020) when using a threshold of 1. Brient et al. (2019) detect a smaller fraction of around 10 % for the same threshold, which is likely due to their analysis of a slightly different cloud regime (strato-cumulus). Denby et al. (2020) used a higher threshold of 2, resulting in a roughly 6 % convective component, which is again similar to our value as well as that Couvreux et al. (2009) found in their sensitivity test.

The properties of the convective and non-convective components also behave as expected. The total moisture flux averaged over the whole convective component decreases the higher the threshold value is set, with the environment compensating most of the upward moisture transport (Figure 5 c). And the higher the threshold is set, the higher the moisture anomaly fluxes in the convective clusters, because the convective area shrinks to cover only the strongest updrafts. In summary, we conclude that the clustering behaves as expected in regards to the total area and moisture fluxes, and that both are strongly and directly affected by the threshold value m_{mask}.

3.2 Cluster size sensitivity

In this section we will focus on the number and size of the clusters. Similar to (e.g. Neggers & Siebesma, 2013; Sulak et al., 2020), we define the cluster size as a typical diameter d, which is calculated by first dividing the volume of a cluster by its vertical ex-

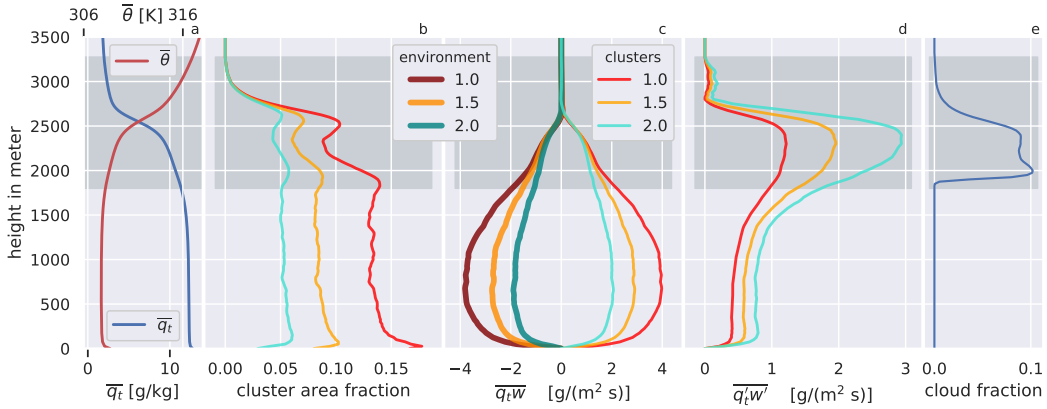

Figure 5. Domain averaged profiles of total water and potential temperature a) and cloud fraction (e) at 13:30 local time, 2016-06-11. The total cluster area (b), total water flux averaged over the full domain (c), and the total water anomaly averaged over the cluster area (e) are shown for 3 different mask thresholds of 1.0,1.5, and 2.0 (mask threshold described in Subsection 2.2).

tent $\triangle z$, which results in a vertically averaged area $A = V/\triangle z$, which we then convert to a diameter d by assuming the area is a circle,

$$d = 2\sqrt{\frac{A}{\pi}} \tag{2}$$

Note that the geometry of the clusters can be very complex, and that the bounding box of the cluster footprint will always exceeds diameter d. Both a perfect cylinder and a convoluted network with many holes will have the same diameter as long as they have the same ratio of volume to vertical extent.

First the simplest case is considered in which the mask and core thresholds (as defined in Section 2.2.2) are almost identical. This makes our clustering approach functionally the same as that used by Brient et al. (2019) to identify updrafts, in which all neighboring convective cells belong to the same cluster. For technical reasons we set the mask threshold to be 0.01 below the core threshold for these tests, and we see that the total number of plumes with a diameter d larger than 100 m increases as the threshold increases (Figure 6). The sudden jump in the largest cluster size between 1 and 1.5 is a good indication that 1 is already close to a critical percolation threshold in which almost the whole convective area is interconnected. This matches the results Brient et al. (2019) show in their supplementary material, where reducing the threshold value to 0.5 leads

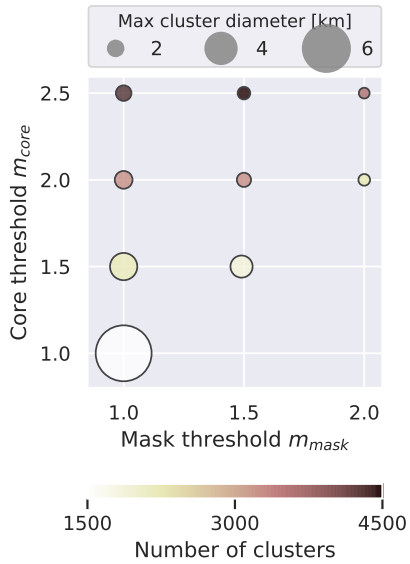

Figure 6. Size of the largest cluster and number of clusters with a diameter larger than 100 m from a single model snapshot at 2016-6-11, 13:30. X and y axis are the values of m_{mask} and m_{core} used for the clustering algorithm. Note that when both values look identical m_{mask} is actually 0.01 smaller m_{core} (e.g m_{mask}=0.99, m_{core}=1.0, details in Subsection 2.2).

to only a few individual clusters remaining. The largest cluster for a mask and core threshold of 1 has a diameter $d > 6$ km, which means that roughly 5 % of the whole boundary layer by volume belongs to a single cluster.

Thanks to the inclusion of the core threshold, we can modify the number and size of the clusters while maintaining the same total volume of convective air. We saw in Figure 4 that increasing the core threshold can lead to clusters either splitting or merging. Our results show that when looking over the whole domain increasing the core threshold both increases the number of plumes and decreases the diameter of the largest plume (Figure 6).

One motivation for taking this approach is that it enables decomposing the contribution to the total flux by plume diameter d (Figure 7). Close to the surface the smaller plumes contribute more, while the contribution of the larger plumes dominates above the cloud base. This configuration is consistent with the behavior of the size-dependent multi plume model framework as proposed by (Neggers, 2015). The core threshold only has a very slight effect on the total flux changes (visible by looking at the 2.0 line in Fig-

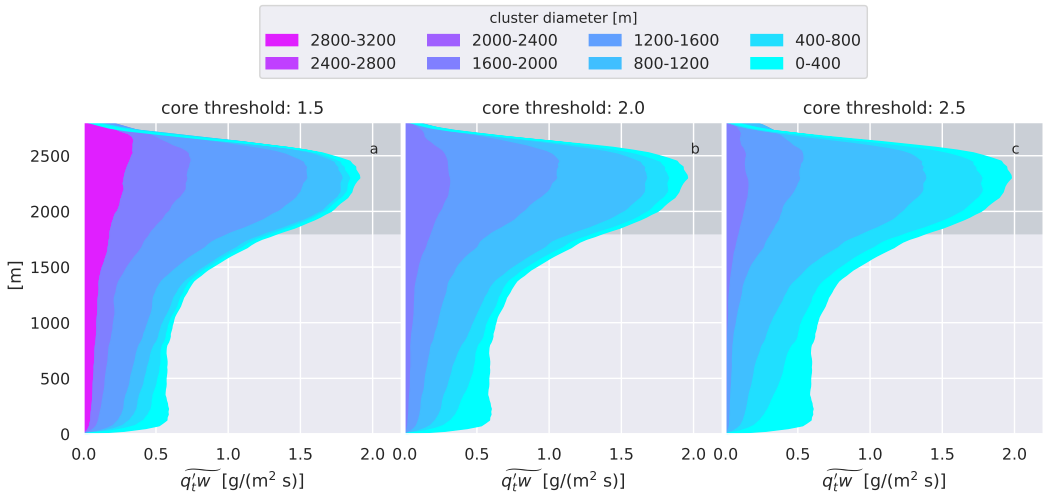

Figure 7. Moisture anomaly fluxes averaged over cluster area at 13:30 local time, 2016-06-11. Flux is decomposed into the contributions of the clusters binned by cluster diameter. All clusters have a mask threshold of 1.5, and differing core thresholds (cluster algorithm described in Section 2.2). The dark background marks the cloud layer.

ure 7). These slight differences result from areas which are convective not forming a cluster if the core threshold is sufficiently high that no core is available to form a cluster, as illustrated by the four bottom left pixels in Figure 3. So while the total flux is weakly affected, the size breakdown varies strongly with the core threshold. For example, if the core and mask threshold are set to 1.5, a single cluster with a diameter of 3 km contributes roughly 15 % of the moisture anomaly transport above cloud base. If the core threshold is increased to 2.0, the widest cluster is under 2 km in diameter.

From these results we can conclude that our clustering approach has fulfilled the four criteria we laid out in Section 2.2. By combining the two thresholds and the watershedding approach we can freely change the total convective area without running the risk of the largest plumes percolating throughout the whole domain, which is a clear benefit of the clustering method adopted here. However, the total number of clusters and their size distribution varies depending on the threshold values chosen, and any quantitative assessment of the clusters needs to take this into account.

For the full analysis of the LASSO cases (to be discussed in the next Section) a mask threshold of 1.5 and a core threshold of 2.0 is adopted. These values were chosen for a number of reasons. Firstly, they avoid routinely detecting clusters with diameters above

2 km, which when looked at individually are often highly non-cohesive. The chosen parameters also avoid a distinct step in size between the largest few clusters and the rest. A mask threshold of 1.0 was discarded because it leads to a large area of air at the inversion height to be classified as convective, causing the cluster area fraction to substantially exceed the cloud fraction throughout the cloud layer (Figure 5). On the other hand, a value of 2.0 was deemed too restrictive, as it masks out areas which seem to still be dominated by convective plumes (Figure 4).

While we determined a suitable pair of threshold values through trial and error, other methods have been proposed, for example by following a flux decomposition (Efstathiou et al., 2020), or by separating Gaussian and non-Gaussian components in joint probability density functions (Chinita et al., 2018). However, it is unclear if these approaches are suitable to identify individual clusters. Another option would be to include more detailed geometric properties of the clusters into the selection process (Denby et al., 2020), but we do not expect a more exhaustive analysis to change our chosen threshold values by more than 0.5.

4 Cluster analysis

In this section we will first take a look at the general properties of all clusters detected by the algorithm, before analyzing various clusters aspects in relationship to the cluster diameter.

4.1 Cluster types

In this subsection we first consider all clusters in a single snapshot at 13:30 local time of the 2016-06-11 case. The goal is to establish if a clear pattern differentiating clusters based on their top height, vertical extent, diameter, and vertical velocity exists in an instantaneous field (Figure 8). Having this knowledge is helpful for interpreting the analysis of multiple fields for 26 cases, as discussed in the next section. Based on the grouping of points in Figure 8 we loosely categorize three distinct types:

- **Type 1** Coherent structures extending down to the surface. These are situated on the diagonal, because their vertical extent equals their top height. These clusters all have positive mean vertical velocities, and the clusters with the largest diameters all belong to this group. Accordingly, these structures adhere to what is

commonly understood to be a "plume", in that they are an interconnected mass of air moving from the surface upwards.

- **Type 2** Clusters not reaching lifting condensation level (LCL) and not connected to the surface. This type generally has a positive vertical velocity, but a small diameter and vertical extent (Figure 8). Because of these aspects this type can be interpreted as representing dry subcloud layer turbulent structures.
- **Type 3** Clusters not connected to the surface but reaching above their LCL. Some of these clusters are quite wide and tall, and they tend to have neutral or negative vertical velocities. Therefore, we assume that these clusters are the decaying remnants of previously active Type 1 plumes, or independent fragments of subsiding shells which split from their plume.

While the characteristics of cluster Types 2 and 3 are certainly interesting in themselves, in the remainder of the paper we choose to focus mainly on Type 1, i.e. plume-like structures connected to the surface, given their strong contribution to vertical transport. Gaining insights in the other types and in life-cycle effects is for now considered a future research topic.

4.2 Cluster height

The next step is to dramatically enhance the sample size of the analysis, by now considering all clusters detected in the simulations of all 26 LASSO cases. This yields a total of 650 3D snapshots, each 30 minutes apart, from 6:30 to 18:00 local time.

First the cluster height is studied as a function of diameter d. All clusters are discarded which i) do not begin in the lowest 100 m or ii) which have diameters or heights smaller than 100 m. This selection still leaves us with 800.000+ clusters. The single snapshot shown in Figure 8 already indicates that a well-defined size-height relationship exists, but with substantial spread. By further improving the sample size by considering 26 days this spread reduces, and the relationship becomes stronger (Fig. 9 a). There is no noticeable change in functionality at any scale, suggesting that there is no fundamental difference between clusters which reach the cloud base and those which do not. This also suggests that the model domain is large enough to not impose an artificial limit on cluster size.

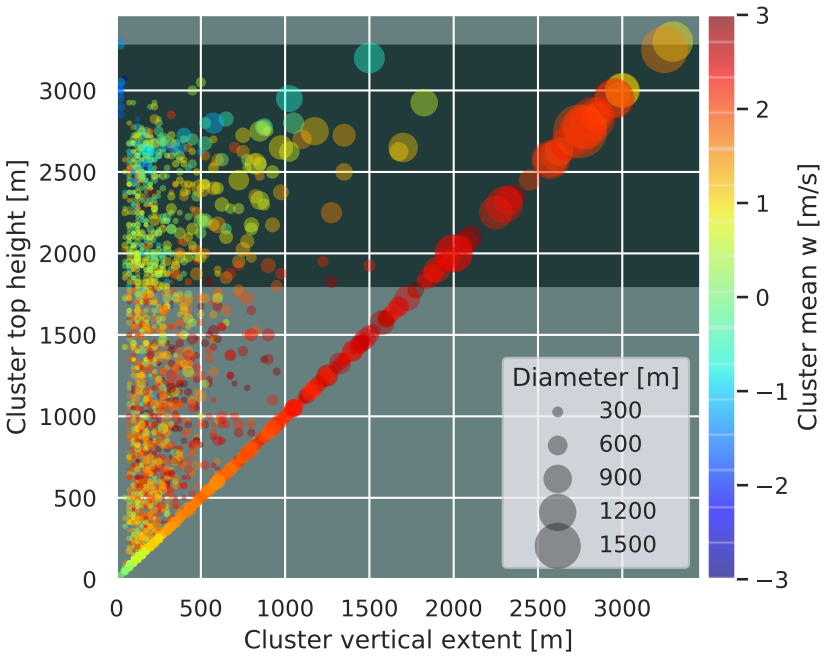

Figure 8. Scatter plot of cluster vertical extent and top height at 13:30, 2016-06-11. The size of each circle marks the average diameter of the cluster, and the color gives the mean vertical velocity averaged over the whole cluster. Clusters along the diagonal have the same top height as vertical extent, meaning that they connect directly to the surface. The darker background marks the cloud layer.

A noticeable feature is a small branch of clusters which are only a few hundred meters high but with diameters up to 1000 m (Figure 9 a). Over 90 % of these flat clusters occur in the morning and evening transition periods, when the boundary layer is not fully convective. While we could easily filter these anomalous clusters out, they are sufficiently rare that they do not substantially affect the average size-height relation, as apparent in this Figure 9, or any other of our analyses.

4.3 Vertical structure

In this subsection we evaluate profiles of cluster area, vertical velocity and humidity. The goal is to determine if these properties also stratify with cluster diameter, and if so, if this stratification is also height dependent. To achieve this clusters are first sorted by diameter, before studying the bin-average properties.

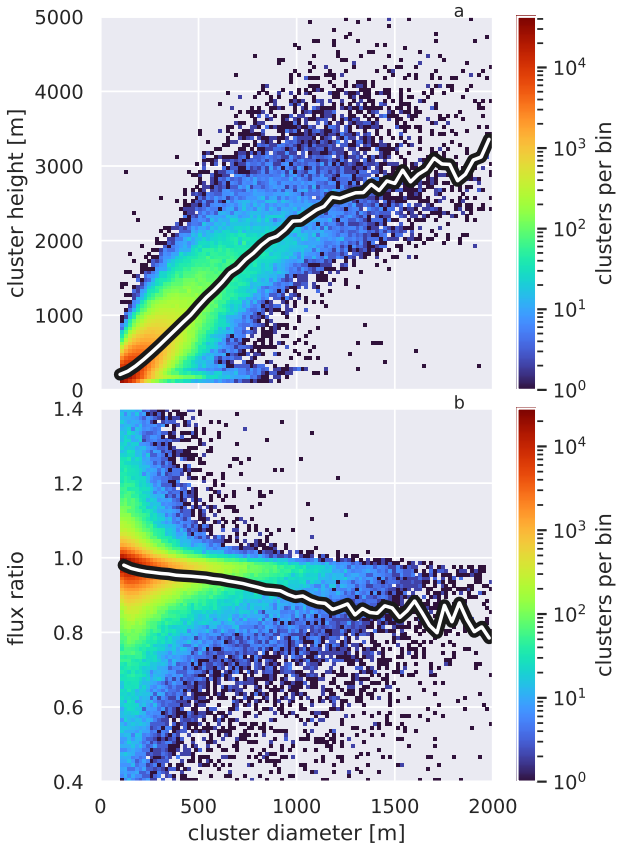

Figure 9. Histograms of cluster diameter vs cluster height (a), and flux ratio (b). All clusters with diameters and vertical extents below 100 m or which do not begin in the lowest 100 m of the domain are filtered out, leaving 801644 Type 1 clusters. The distinct branch of wide but low clusters visible in panel a) is discussed in Subsection 4.2). The flux ratio F_{top}/F_{ref} shown in panel b) is the ratio of the integrated vertical moisture flux approximated through the top hat approach, divided by the flux of the 3D cluster (Equation 3, Subsection 4.4). The white line marks the average value over all clusters in that diameter bin.

4.3.1 Two bin analysis

The first exploratory step is to consider cluster properties of only two bins, 400-600 and 1200-1600 m (Figure 10). The goal here is to understand not only the bin-average behavior, but also the bin-internal variability that might exist. As there are only about 10 clusters per snapshot that fall within the 1200-1600 bin, we include clusters from 3 consecutive snapshots (13:00, 13:30, 14:00). The 30 minutes time delay between the snapshots is sufficiently long that any cluster will have evolved substantially over time, so that all clusters can be considered independent. Consistent with the results from the last subsection, we find that the wider clusters also reach higher (Figure 10). Most (i.e. 26 of 28) larger clusters terminate close to cloud layer top, with only two reaching just above cloud base. In contrast, the vast majority of the smaller clusters end below the cloud base, with a few noticeable outliers reaching up to 2500 m.

The area profiles of the individual clusters vary quite strongly with height. This complicates calculating a meaningful bin-average. The easiest approach is to average over all plumes present at each height (e.g. Neggers, 2015). While this works well when all profiles have a similar vertical extent, if the individual profiles have strongly varying top heights this means that ensemble effects enter the mean. In that case the top of the mean profile is only based on the small minority of clusters which reach that high (a heavy "survivor bias"). This averaging method, here referred to as ***"mean-avail"***, is commonly used in conditional sampling studies of cumulus cloud fields. A simple alternative is to average over all clusters at all heights, by extending the cluster profiles beyond their top height with a meaningful reference value. For cluster area this is zero, while for state variables these can be domain averages. This method, here labeled ***"mean-all"***, would be particularly useful for considering cluster contributions to flux profiles.

For the small clusters in the 400-600 m bin, switching from main-avail to mean-all leads to a gradual decrease in diameter d above the half-way mark of their vertical extent, at about 500 m height, see Figure 10 a). This expresses that in the top half a strong variation in cluster top height exists. In contrast, for the large clusters both mean-avail and mean-all are very similar throughout most of the profile. First the mean diameter increases up to cloud base, and stays more or less constant from 1500 m to 2500 m height. Above 2500 m, the mean-all decreases to zero, while the mean-avail does not drop below 450 m.

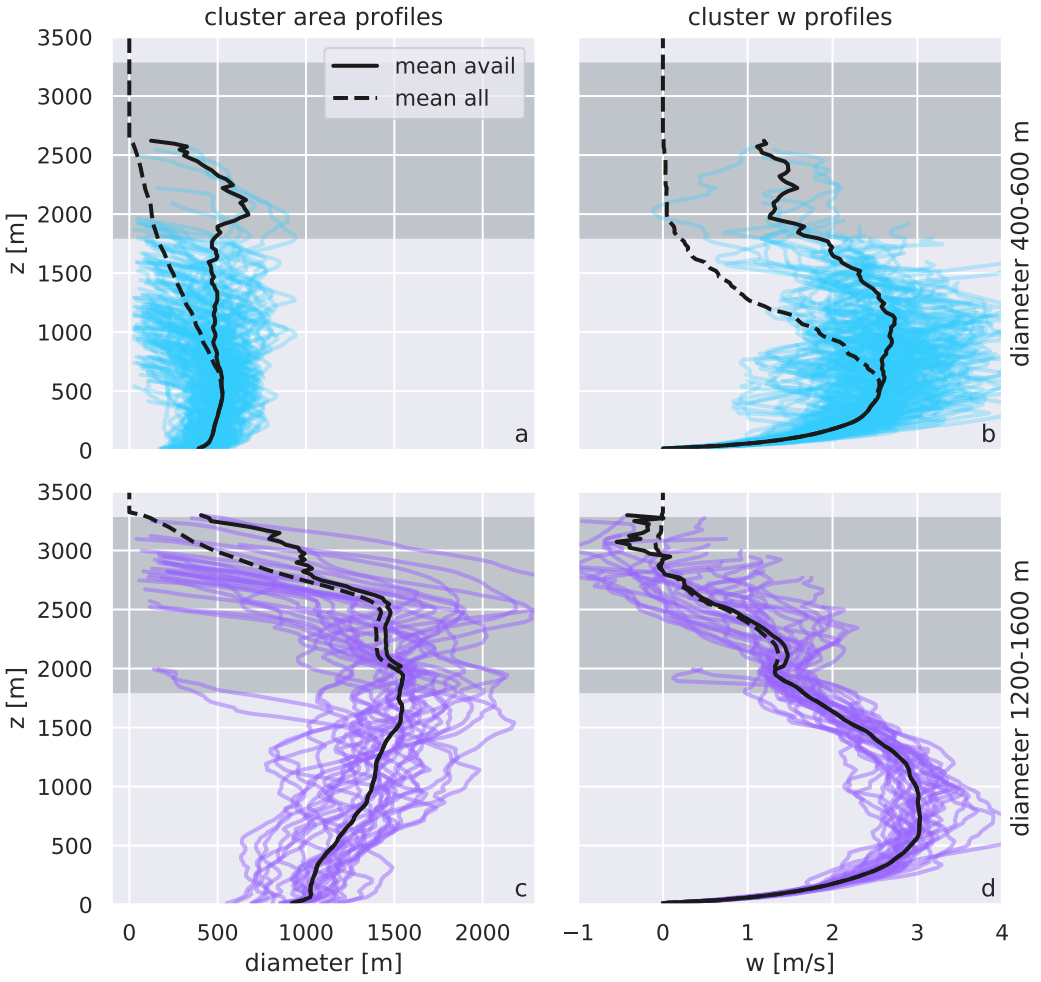

Figure 10. Mean area in diameter (left), and vertical velocity (right) profiles of 141 Type 1 clusters with an average diameter between 200 and 400 me (top), and 28 clusters with an average diameter between 1200-1600 m (bottom). All clusters are included which begin below 100 m, and are taken from 3 snapshots at 13:00, 13:30, and 14:00 local time. Dark grey background marks cloud layer at 13:30. The average over all profiles at that height is labeled "mean avail", while "mean all" represents clusters that do not reach that height with a value of 0. Note that for Subfigures a and c the mean diameter is calculated by first calculating the average area of the clusters, and then converting that area to a diameter.

Concerning vertical velocity w, for both the small and large clusters the mean profile below cloud base displays the typical feature of a surface driven free convective layer, with a peak velocity reached slightly below the half-way height. In that sense these profiles conform to the classic model for a rising buoyancy-driven moist plume (e.g. Simpson & Wiggert, 1969). A brief acceleration above cloud base can be distinguished in both bins, associated with latent heat release due to condensation. However, significant differences also exist. While the velocity profiles of the smaller clusters begin very similar to those of the larger clusters, it peaks at a smaller value (2.5 m s^{-1} versus 3 m s^{-1}). In addition, most of the smaller clusters stop quite far below cloud base, although a few do reach condensation. What stands out is that the spread among the smaller clusters is larger, in the amplitude of w but also in their top height (as discussed before). The latter is expressed in the more significant difference between mean-avail w and mean-all w for the smaller clusters, which also starts at a much lower height. The small spread among the larger plumes suggests that the rising plume model is in principle more applicable to the larger size category than the smaller clusters.

4.3.2 Multi bin analysis

After analysing of two size bins at the extremes of the cluster distribution, we now consider the full spectrum (Figure 11). To also capture the time evolution, all plumes during three mid-day time periods of the 11 June 2016 case are included. The one hour time periods containing three snapshots were again chosen to enhance sample size.

We find that at all three timepoints, the profile of mean-all Type 1 cluster area is a smooth function of bin size. The smaller the bin, the quicker the cluster diameter decreases with height towards cloud base. This changes into an increasing diameter with height for the largest sized clusters. Above cloud base, the area quasi-linearly decreases to zero near cloud top for all bins. Over the 5 hours shown, the effect of boundary layer deepening is visible in the higher extent of the clusters and in the more pronounced acceleration above cloud base. Over time more larger clusters emerge, with diameters exceeding 1400 m. This diurnal increase in the largest cluster size is consistent with the recent findings of van Laar et al. (2019). Note that the strong variability that still exists among the largest cluster bins suggests that sample size is still limited.

514 At all 3 times of day the vertical velocity w and the total specific humidity anomaly
515 q_t' shows only weak size dependence below cloud base in bins larger than 1000 m (Fig-
516 ure 11). However, above cloud base significant size dependence exists. For w this sig-
517 nal is still somewhat overshadowed by sampling noise, but for q_t' this stratification as a
518 function of size is well defined and much stronger. This size-stratification in both vari-
519 ables is the reason why the largest clusters contribute so much to the moisture flux above
520 cloud base (shown in Figure 7). This seems more due to their high moisture anomalies
521 than their vertical velocities. For interpreting these profiles it is important to keep in mind
522 that the profiles of the smaller bins (600 m and below) smoothly approach zero because
523 the clusters have a wide variability in termination heights (as shown in Figure 10).

524 ### 4.4 Plume-internal variability

525 The often-used "top hat approach" in plume modeling (e.g. Davidson, 1986; Wang
526 & Stevens, 2000) assumes that its internal structure is horizontally homogeneous, ne-
527 glecting the variability inside the plume. In this subsection we attempt to quantify the
528 error resulting from applying the top hat assumption to the clusters. Chinita et al. (2018)
529 also attempted to quantify this error, but our approach differs in two crucial aspects. Firstly,
530 we again separate the clusters by their diameter, and secondly instead of looking at the
531 profile we will integrate the flux over the whole cluster to only compare a single value
532 per cluster. We take this approach to allow us to include all clusters from all simulations
533 into a single comparison (Figure 9 b). The reference flux F_{ref} is the integral over the
534 total water anomaly flux, which can be computed from the average over the total wa-
535 ter anomaly times the vertical velocity at each level (the tilde marks an average over the
536 cluster):

$$F_{ref} = \int \widetilde{q_t'w'} A \, dz \qquad F_{top} = \int \widetilde{q_t'}\widetilde{w'} A \, dz \tag{3}$$

537 The simplified top hat flux F_{top} replaces the horizontal integral with the anomalies of
538 w and q_t averaged over the cluster, multiplied with the area A of the cluster at that height.
539 A ratio above 1 means that by neglecting the horizontal covariances within the cluster
540 the top hat simplification overestimates the flux, and below 1 signals an underestima-
541 tion.

542 The results are shown in Figure 9 b. For this analysis we only look at Type 1 clus-
543 ters that begin below 100 m, and have both a diameter and vertical extent higher than

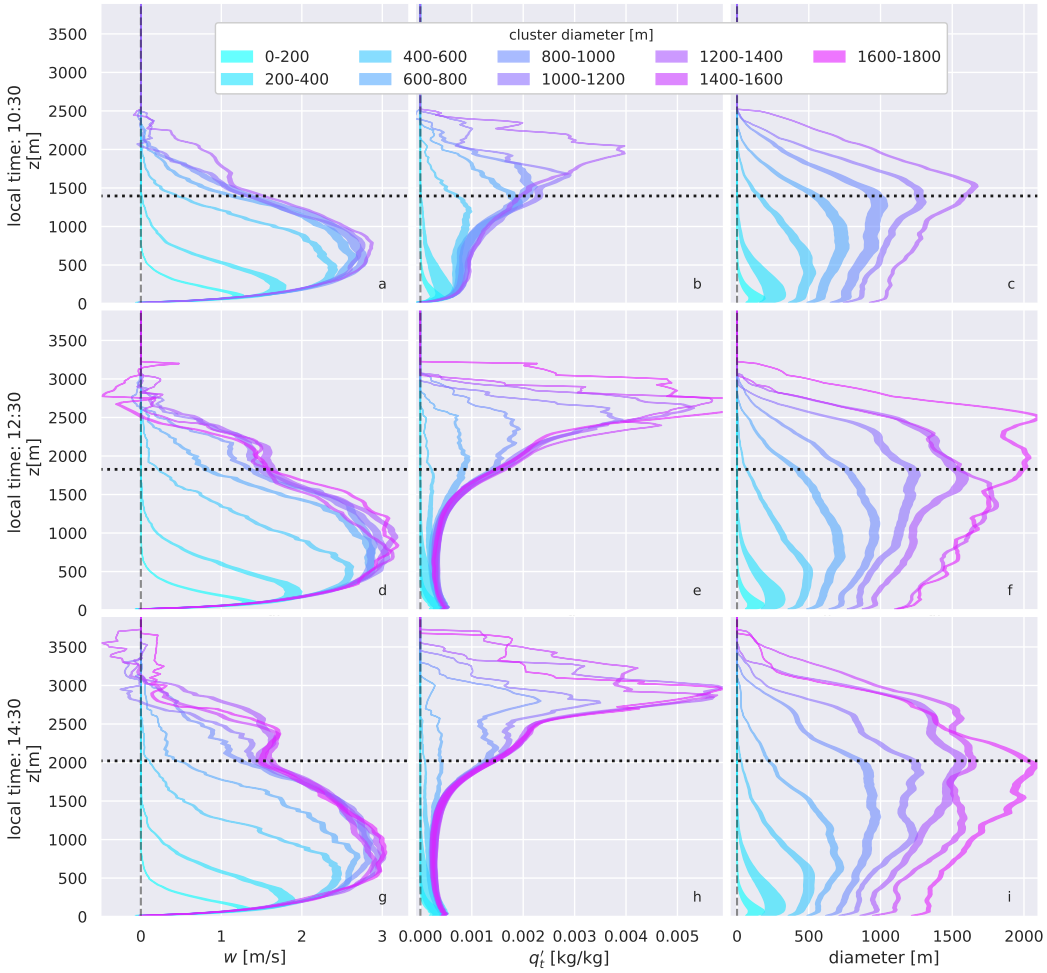

Figure 11. Mean-all vertical velocity, moisture anomaly, and diameter profiles of Type 1 clusters beginning in the lowest 100 m on the 2016-06-11 (see in Figure 10 for a description of mean-all, and Figure 8 for Type 1). The horizontal dotted line marks cloud base. Each row represents a different time period, including 10:00-11:00 (top), 12:00-13:00 (middle) and 14:00-15:00 (bottom). The width of the lines indicates the total area covered by all clusters in that specific bin at each height level.

100 m, which still leaves us with over 800,000 clusters. While the thinnest clusters with diameters below 500 m have a wide spread in ratios above and below 1, clusters wider than 1000 m very rarely have a ratio above 1. While there is a substantial spread for the thinnest clusters, the logarithmic coloring used in Figure 9 shows that there is a very clear peak in the distribution between 1.0 and 0.95 up until roughly 750 meters. At these ranges the mean and the median match quite closely. Above 1000 m the most likely ratio remains near 0.95, but with almost no ratios above 1 and a sizeable number of ratios between 0.4 and 0.8, the mean drops lower than the median. For the largest clusters between 1.5 and 2 km in diameter the flux underestimation ranges between 15 and 20 %. We were surprised to see how closely a linear relationship matches the data, suggesting that on average the impact of plume-internal variability on its flux is directly linked to the cluster width. That the highest underestimation occurs in the largest clusters can in part be explained by the findings of Chinita et al. (2018), who reported that the covariances increase with distance from cloud base. And given that the wider clusters extend higher (see Figure 9 a), our results agree well with those of Chinita et al. (2018).

5 Discussion and Summary

5.1 Discussion

The results obtained by our clustering analysis of coherent structures in the moist convective boundary layer can inform the development and evaluation of convection schemes consisting of a size-spectrum of plumes (Arakawa & Schubert, 1974; Neggers, 2015; Brast et al., 2018; Sakradzija & Klocke, 2018; Hagos et al., 2018; Olson et al., 2019). The well-defined size-height relationship we find strongly supports the spectral basis of these schemes. In addition, the persistent and frequent occurrence of surface-rooted plume-like structures in many independent 3D snapshots, in combination with their significant contribution to transport, further supports use of the classic rising plume model as part of such schemes (Simpson & Wiggert, 1969).

Apart from these encouraging findings, new insights into the vertical structure of these Type 1 clusters were also obtained that call for caution in applying some often-made assumptions in plume models. First and foremost is the assumption of a constant plume area with height, which is sometimes used as a practical simplification (e.g. Neggers, 2015; Suselj et al., 2019). We find strong height dependence in the plume area. While

vertical velocity and moisture anomalies also show size dependence, this pales in comparison to the plume diameter. The way plume profiles change with height also strongly depends on plume diameter; small plumes behave substantially different in that respect compared to large plumes, featuring significant loss of collective mass while still traveling upward. In contrast, larger clusters gain mass up to the cloud base, above which they shed it in a quasi-linear way, at least for the SGP cases studied. These clear signals motivate and support the use of aggregate plume models in which the area can change with height (e.g. Pergaud et al., 2009; Tan et al., 2018). Larger plumes should widen from the surface to cloud base, and smaller plumes should decrease in width with height.

Note that these height dependencies are still aggregates, in that they represent bin-averages over many plumes in a similar size category. This means that ensemble effects such as the survivor-bias can at least partially explain the effective height dependence. Insight into this process was provided by contrasting the mean-avail with the mean-all averaging methods. On the other hand, the analysis of individual plumes (Figure 10) indicates that also single large coherent structures tend to gain mass, mainly in the lower half of the convective layer but especially close to the surface. Our method does not provide information on how such clusters gain and shed mass. In other words, we can not distinguish between clusters loosing mass to the environment or to other (larger) clusters. It also remains unclear to which degree the larger clusters grow by incorporating smaller clusters or entraining air from the environment. These are valid questions to ask when interested in how plumes of different sizes exchange mass, which is part of some predator-prey type convection schemes (e.g. Wagner & Graf, 2010; Hagos et al., 2018). Gaining insight into these processes requires further research.

Impacts on vertical transport were also investigated. While we find that the height-dependence in plume area contributes significantly to the net flux profile, our results also provide information about the often-used top-hat approach in convective modeling. Although the potential errors resulting from this assumption can be large for individual clusters, on average the top hat approach only weakly underestimates moisture fluxes, between 0 and maximally 20 %. This underestimation scales in a well-defined and linear way with the cluster diameter, which in principle facilitates accounting for this behavior in models.

606 ### 5.2 Summary

607 A clustering method is applied to high resolution simulations of shallow cumulus
608 convection over land to investigate the size dependence of coherent structures in the con-
609 vective boundary layer. Our two-threshold clustering approach successfully identifies in-
610 dividual coherent structures, further supporting the popular use of a surface tracer to
611 efficiently study convection via LES as first proposed by (Couvreux et al., 2009). The
612 two main free parameters of the algorithm have the desired effect of i) control over the
613 total volume of convective clusters, ii) independent core masking, iii) consistency with
614 previously proposed methods in terms of area profiles.

615 Using this clustering method, the behavior of more than 800k coherent structures
616 in 26 LASSO simulations at the ARM SGP site was investigated. The insights on clus-
617 ter behavior obtained in this study can guide the development and evaluation of in par-
618 ticular spectral convection schemes. The main findings can be briefly summarized as fol-
619 lows:

620 - Surface-rooted coherent structures resembling plumes are frequently and persis-
621 tently present in instantaneous 3D snapshots;
622 - There is a well-defined and strong relationship between the vertical extent and di-
623 ameter of these clusters;
624 - The vertical velocity profile of larger clusters matches that expected from the clas-
625 sic buoyancy-driven plume model (Simpson & Wiggert, 1969), including latent heat
626 effects above cloud base.
627 - Smaller clusters have positive vertical velocities all the way up to their tops, but
628 feature substantial variation in top heights;
629 - A strong size dependence also exists in the vertical structure of aggregate plume
630 diameter. While smaller clusters have decreasing diameter with height below cloud
631 base, larger clusters have increasing diameter;
632 - The size dependence in vertical velocity and total water content is largest above
633 cloud base, but much weaker in the subcloud layer;
634 - The top hat approach can explain between 80-100 % of the cluster transport, the
635 underestimation increases linearly with cluster diameter.

Acknowledgments

This research was supported primarily by the U.S. Department of Energy's Atmospheric System Research, an Office of Science Biological and Environmental Research program, under grant DE-SC0017999 awarded to Thijs Heus. Our research would not have been possible without the ground work laid by the LASSO project (LES ARM Symbiotic Simulation and Observation) and the Southern Great Plains (ARM-SGP) atmospheric observatory established by the Atmospheric Radiation Measurement (ARM) user facility. The computing resources to run the simulations were provided by a Cleveland State University Faculty Research and Development award.

The full 3D snapshots of the model fields and clusters are too large to be made easily accessible ($\approx$ 150 GB per day), but the mean properties and profiles of all clusters are freely available at `10.5281/zenodo.4744600`. The simulations were generated with version 1.9.1 of MicroHH `https://github.com/microhh/microhh2/releases/tag/1.9.1`. The data used to force MicroHH and to evaluate the simulated cloud fraction and base are available through the LASSO bundle browser `https://adc.arm.gov/lassobrowser`.

References

Arakawa, A., & Schubert, W. H. (1974, April). Interaction of a cumulus cloud ensemble with the large-scale environment, part I. *Journal of the Atmospheric Sciences*, *31*(3), 674–701. doi: 10.1175/1520-0469(1974)031⟨0674:ioacce⟩2.0.co;2

Baba, Y. (2020, March). Shallow convective closure in a spectral cumulus parameterization. *Atmospheric Research*, *233*, 104707. doi: 10.1016/j.atmosres.2019.104707

Benner, T. C., & Curry, J. A. (1998, November). Characteristics of small tropical cumulus clouds and their impact on the environment. *Journal of Geophysical Research: Atmospheres*, *103*(D22), 28753–28767. doi: 10.1029/98jd02579

Brast, M., Schemann, V., & Neggers, R. A. J. (2018). Investigating the Scale Adaptivity of a Size-Filtered Mass Flux Parameterization in the Gray Zone of Shallow Cumulus Convection. *Journal of the Atmospheric Sciences*, *75*(4), 1195–1214. doi: 10.1175/JAS-D-17-0231.1

Brient, F., Couvreux, F., Villefranque, N., Rio, C., & Honnert, R. (2019, March). Object-oriented identification of coherent structures in large eddy simulations:

Importance of downdrafts in stratocumulus. *Geophysical Research Letters*, *46*(5), 2854–2864. doi: 10.1029/2018gl081499

Brown, A. R., Cederwall, R. T., Chlond, A., Duynkerke, P. G., Golaz, J. C., Khairoutdinov, M., ... Stevens, B. (2002). Large-eddy simulation of the diurnal cycle of shallow cumulus convection over land. *Quart. J. Roy. Meteor. Soc.*, *128*(582), 1075–1093. doi: 10.1256/003590002320373210

Chinita, M. J., Matheou, G., & Teixeira, J. (2018, February). A Joint Probability Density–Based Decomposition of Turbulence in the Atmospheric Boundary Layer. *Monthly Weather Review*, *146*(2), 503–523. doi: 10.1175/MWR-D-17-0166.1

Cohen, Y., Lopez-Gomez, I., Jaruga, A., He, J., Kaul, C. M., & Schneider, T. (2020, September). Unified Entrainment and Detrainment Closures for Extended Eddy-Diffusivity Mass-Flux Schemes. *J. Adv. Model. Earth Syst.*, *12*(9). doi: 10.1029/2020MS002162

Couvreux, F., Hourdin, F., & Rio, C. (2009, December). Resolved versus parametrized boundary-layer plumes. Part I: A parametrization-oriented conditional sampling in large-eddy simulations. *Boundary-Layer Meteorology*, *134*(3), 441–458. doi: 10.1007/s10546-009-9456-5

Davidson, G. (1986). Gaussian versus top-hat profile assumptions in integral plume models. *Atmospheric Environment (1967)*, *20*(3), 471-478. Retrieved from `https://www.sciencedirect.com/science/article/pii/0004698186900879` doi: https://doi.org/10.1016/0004-6981(86)90087-9

Dawe, J. T., & Austin, P. H. (2012, January). Statistical analysis of an LES shallow cumulus cloud ensemble using a cloud tracking algorithm. *Atmospheric Chemistry and Physics*, *12*(2), 1101–1119. doi: 10.5194/acp-12-1101-2012

Denby, L., Böing, S. J., Parker, D. J., Ross, A. N., & Tobias, S. M. (2020, August). The effect of ambient shear on coherent boundary layer structures. *arXiv:2008.07217 [physics]*.

Efstathiou, G. A., Thuburn, J., & Beare, R. J. (2020, January). Diagnosing Coherent Structures in the Convective Boundary Layer by Optimizing Their Vertical Turbulent Scalar Transfer. *Boundary-Layer Meteorol*, *174*(1), 119–144. doi: 10.1007/s10546-019-00480-1

Ghate, V. P., Miller, M. A., & DiPretore, L. (2011). Vertical velocity struc-

ture of marine boundary layer trade wind cumulus clouds. *Journal of Geophysical Research: Atmospheres*, *116*(D16). Retrieved from https://agupubs.onlinelibrary.wiley.com/doi/abs/10.1029/2010JD015344 doi: https://doi.org/10.1029/2010JD015344

Grabowski, W. W., Bechtold, P., Cheng, A., Forbes, R., Halliwell, C., Khairoutdinov, M., ... Xu, K.-M. (2006). Daytime convective development over land: A model intercomparison based on LBA observations. *Quarterly Journal of the Royal Meteorological Society*, *132*(615), 317–344. doi: 10.1256/qj.04.147

Griewank, P. J., Heus, T., Lareau, N. P., & Neggers, R. A. J. (2020, April). *Size-dependence in chord characteristics from simulated and observed continental shallow cumulus* (Preprint). Clouds and Precipitation/Atmospheric Modelling/Troposphere/Physics (physical properties and processes). doi: 10.5194/acp-2020-338

Gustafson, W. I., Vogelmann, A. M., Cheng, X., Endo, S., Johnson, K. L., Krishna, B., ... Xiao, H. (2017). Atmospheric Radiation Measurement (ARM) Research Facility. LASSO Data Bundles. Southern Great Plains Central Facility (C1). *ARM Data Archive: Oak Ridge, Tennessee, USA.*. doi: http://dx.doi.org/10.5439/1342961

Gustafson, W. I., Vogelmann, A. M., Li, Z., Cheng, X., Dumas, K. K., Endo, S., ... Xiao, H. (2020). The large-eddy simulation (les) atmospheric radiation measurement (arm) symbiotic simulation and observation (lasso) activity for continental shallow convection. *Bulletin of the American Meteorological Society*, *101*(4), E462 - E479. Retrieved from https://journals.ametsoc.org/view/journals/bams/101/4/bams-d-19-0065.1.xml doi: 10.1175/BAMS-D-19-0065.1

Hagos, S., Feng, Z., Plant, R. S., Houze, R. A., & Xiao, H. (2018, February). A stochastic framework for modeling the population dynamics of convective clouds. *Journal of Advances in Modeling Earth Systems*, *10*(2), 448–465. doi: 10.1002/2017ms001214

Hernandez-Deckers, D., & Sherwood, S. C. (2016, October). A numerical investigation of cumulus thermals. *Journal of the Atmospheric Sciences*, *73*(10), 4117–4136. doi: 10.1175/jas-d-15-0385.1

Heus, T., Jonker, H. J. J., Van den Akker, H. E. A., Griffith, E. J., Koutek, M., &

Post, F. H. (2009). A statistical approach to the life cycle analysis of cumulus clouds selected in a virtual reality environment. *Journal of Geophysical Research: Atmospheres*, *114*(D6). doi: 10.1029/2008JD010917

Heus, T., & Seifert, A. (2013, August). Automated tracking of shallow cumulus clouds in large domain, long duration large eddy simulations. *Geoscientific Model Development*, *6*(4), 1261–1273. doi: 10.5194/gmd-6-1261-2013

Kleiss, J. M., Riley, E. A., Long, C. N., Riihimaki, L. D., Berg, L. K., Morris, V. R., & Kassianov, E. (2018). Cloud area distributions of shallow cumuli: A new method for ground-based images. *Atmosphere*, *9*(7). Retrieved from `https://www.mdpi.com/2073-4433/9/7/258` doi: 10.3390/atmos9070258

Lamer, K., & Kollias, P. (2015). Observations of fair-weather cumuli over land: Dynamical factors controlling cloud size and cover. *Geophysical Research Letters*, *42*(20), 8693-8701. Retrieved from `https://agupubs.onlinelibrary.wiley.com/doi/abs/10.1002/2015GL064534` doi: https://doi.org/10.1002/2015GL064534

Lareau, N. P. (2020, March). Subcloud and cloud-base latent heat fluxes during shallow cumulus convection. *Journal of the Atmospheric Sciences*, *77*(3), 1081–1100. doi: 10.1175/jas-d-19-0122.1

Lareau, N. P., Zhang, Y., & Klein, S. A. (2018, July). Observed boundary layer controls on shallow cumulus at the ARM southern great plains site. *Journal of the Atmospheric Sciences*, *75*(7), 2235–2255. doi: 10.1175/jas-d-17-0244.1

Lopez-Gomez, I., Cohen, Y., He, J., Jaruga, A., & Schneider, T. (2020, November). A Generalized Mixing Length Closure for Eddy-Diffusivity Mass-Flux Schemes of Turbulence and Convection. *J. Adv. Model. Earth Syst.*, *12*(11). doi: 10.1029/2020MS002161

Neggers, R. A. J. (2015, December). Exploring bin-macrophysics models for moist convective transport and clouds. *Journal of Advances in Modeling Earth Systems*, *7*(4), 2079–2104. doi: 10.1002/2015ms000502

Neggers, R. A. J., Jonker, H. J. J., & Siebesma, A. P. (2003, April). Size statistics of cumulus cloud populations in large-eddy simulations. *Journal of the Atmospheric Sciences*, *60*(8), 1060–1074. doi: 10.1175/1520-0469(2003)60⟨1060:ssoccp⟩2.0.co;2

Neggers, R. A. J., & Siebesma, A. P. (2013, September). Constraining a System of

Interacting Parameterizations through Multiple-Parameter Evaluation: Tracing a Compensating Error between Cloud Vertical Structure and Cloud Overlap. *Journal of Climate*, *26*(17), 6698–6715. doi: 10.1175/jcli-d-12-00779.1

Neggers, R. A. J., Siebesma, A. P., & Heus, T. (2012, September). Continuous single-column model evaluation at a permanent meteorological supersite. *Bulletin of the American Meteorological Society*, *93*(9), 1389–1400. doi: 10.1175/bams-d-11-00162.1

Olson, J. B., Kenyon, J. S., Angevine, W. A., Brown, J. M., Pagowski, M., & Sušelj, K. (2019). *A Description of the MYNN-EDMF Scheme and the Coupling to Other Components in WRF–ARW*. Earth System Research Laboratory (U.S.), Global Systems Division. doi: 10.25923/N9WM-BE49

Park, S.-B., Böing, S., & Gentine, P. (2018, January). Role of Surface Friction on Shallow Nonprecipitating Convection. *J. Atmos. Sci.*, *75*(1), 163–178. doi: 10.1175/JAS-D-17-0106.1

Park, S.-B., Gentine, P., Schneider, K., & Farge, M. (2016, April). Coherent Structures in the Boundary and Cloud Layers: Role of Updrafts, Subsiding Shells, and Environmental Subsidence. *Journal of the Atmospheric Sciences*, *73*(4), 1789–1814. doi: 10.1175/JAS-D-15-0240.1

Pergaud, J., Masson, V., Malardel, S., & Couvreux, F. (2009, July). A Parameterization of Dry Thermals and Shallow Cumuli for Mesoscale Numerical Weather Prediction. *Boundary-Layer Meteorol*, *132*(1), 83–106. doi: 10.1007/s10546-009-9388-0

Peters, J. M., Morrison, H., Varble, A. C., Hannah, W. M., & Giangrande, S. E. (2020, November). Thermal Chains and Entrainment in Cumulus Updrafts. Part II: Analysis of Idealized Simulations. *Journal of the Atmospheric Sciences*, *77*(11), 3661–3681. doi: 10.1175/JAS-D-19-0244.1

Peters, J. M., Nowotarski, C. J., & Mullendore, G. L. (2020, April). Are supercells resistant to entrainment because of their rotation? *Journal of the Atmospheric Sciences*, *77*(4), 1475–1495. doi: 10.1175/JAS-D-19-0316.1

Plank, V. G. (1969, February). The size distribution of cumulus clouds in representative florida populations. *Journal of Applied Meteorology*, *8*(1), 46–67. doi: 10.1175/1520-0450(1969)008⟨0046:tsdocc⟩2.0.co;2

Romps, D. M., & Kuang, Z. (2010, May). Nature versus Nurture in Shallow Con-

vection. *Journal of the Atmospheric Sciences*, *67*(5), 1655–1666. doi: 10.1175/2009JAS3307.1

Romps, D. M., & Öktem, R. (2018, December). Observing clouds in 4d with multiview stereophotogrammetry. *Bulletin of the American Meteorological Society*, *99*(12), 2575–2586.

Sakradzija, M., & Klocke, D. (2018). Physically Constrained Stochastic Shallow Convection in Realistic Kilometer-Scale Simulations. *Journal of Advances in Modeling Earth Systems*, *10*(11), 2755–2776. doi: 10.1029/2018MS001358

Sakradzija, M., Seifert, A., & Heus, T. (2015). Fluctuations in a quasi-stationary shallow cumulus cloud ensemble. *Nonlinear Processes in Geophysics*, *22*(1), 65–85. doi: 10.5194/npg-22-65-2015

Sherwood, S. C., Bony, S., & Dufresne, J.-L. (2014, January). Spread in model climate sensitivity traced to atmospheric convective mixing. *Nature*, *505*(7481), 37–42. doi: 10.1038/nature12829

Siebesma, A. P., Bretherton, C. S., Brown, A., Chlond, A., Cuxart, J., Duynkerke, P. G., ... Stevens, D. E. (2003). A large eddy simulation intercomparison study of shallow cumulus convection. *J. Atmos. Sci.*, *60*(10), 1201–1219. doi: 10.1175/1520-0469(2003)60

Siebesma, A. P., Soares, P. M. M., & Teixeira, J. (2007, April). A Combined Eddy-Diffusivity Mass-Flux Approach for the Convective Boundary Layer. *Journal of the Atmospheric Sciences*, *64*(4), 1230–1248. doi: 10.1175/JAS3888.1

Simpson, J., & Wiggert, V. (1969, July). Models odf precipitating cumulus towers. *Monthly Weather Review*, *97*(7), 471–489. doi: 10.1175/1520-0493(1969)097⟨0471:mopct⟩2.3.co;2

Sulak, A. M., Calabrase, W. J., Ryan, S. D., & Heus, T. (2020). The contributions of shear and turbulence to cloud overlap for cumulus clouds. *Journal of Geophysical Research: Atmospheres*, *125*(10), e2019JD032017. Retrieved from `https://agupubs.onlinelibrary.wiley.com/doi/abs/10.1029/2019JD032017` (e2019JD032017 10.1029/2019JD032017) doi: https://doi.org/10.1029/2019JD032017

Suselj, K., Kurowski, M. J., & Teixeira, J. (2019, February). On the factors controlling the development of shallow convection in eddy-diffusivity/mass-flux models. *Journal of the Atmospheric Sciences*, *76*(2), 433–456. doi:

10.1175/jas-d-18-0121.1

Tan, Z., Kaul, C. M., Pressel, K. G., Cohen, Y., Schneider, T., & Teixeira, J. (2018, March). An Extended Eddy-Diffusivity Mass-Flux Scheme for Unified Representation of Subgrid-Scale Turbulence and Convection. *J. Adv. Model. Earth Syst.*, *10*(3), 770–800. doi: 10.1002/2017MS001162

van Heerwaarden, C. C., van Stratum, B. J. H., Heus, T., Gibbs, J. A., Fedorovich, E., & Mellado, J. P. (2017, August). MicroHH 1.0: A computational fluid dynamics code for direct numerical simulation and large-eddy simulation of atmospheric boundary layer flows. *Geoscientific Model Development*, *10*(8), 3145–3165. doi: 10.5194/gmd-10-3145-2017

van Laar, T. W., Schemann, V., & Neggers, R. A. J. (2019, March). Investigating the Diurnal Evolution of the Cloud Size Distribution of Continental Cumulus Convection Using Multiday LES. *Journal of the Atmospheric Sciences*, *76*(3), 729–747. doi: 10.1175/jas-d-18-0084.1

Vial, J., Bony, S., Dufresne, J.-L., & Roehrig, R. (2016). Coupling between lower-tropospheric convective mixing and low-level clouds: Physical mechanisms and dependence on convection scheme. *J. Adv. Model Earth Syst.*, *8*(4), 1892–1911. doi: 10.1002/2016MS000740

Wagner, T. M., & Graf, H.-F. (2010). An ensemble cumulus convection parameterization with explicit cloud treatment. *Journal of the Atmospheric Sciences*, *67*(12), 3854 - 3869. Retrieved from `https://journals.ametsoc.org/view/journals/atsc/67/12/2010jas3485.1.xml` doi: 10.1175/2010JAS3485.1

Wang, S., & Stevens, B. (2000). Top-hat representation of turbulence statistics in cloud-topped boundary layers: A large eddy simulation study. *Journal of the Atmospheric Sciences*, *57*(3), 423 - 441. Retrieved from `https://journals.ametsoc.org/view/journals/atsc/57/3/1520-0469_2000_057_0423_throts_2.0.co_2.xml` doi: 10.1175/1520-0469(2000)057⟨0423:THROTS⟩2.0.CO;2

Wood, R., & Field, P. R. (2011, September). The distribution of cloud horizontal sizes. *Journal of Climate*, *24*(18), 4800–4816. doi: 10.1175/2011jcli4056.1

Yanai, M., Esbensen, S., & Chu, J.-H. (1973, May). Determination of Bulk Properties of Tropical Cloud Clusters from Large-Scale Heat and Moisture Budgets. *Journal of Atmospheric Sciences*, *30*(4), 611–627. doi:

866 10.1175/1520-0469(1973)030⟨0611:DOBPOT⟩2.0.CO;2

867 Zheng, Y., Rosenfeld, D., & Li, Z. (2021). Sub-cloud turbulence explains cloud-base
868 updrafts for shallow cumulus ensembles: First observational evidence. *Geo-*
869 *physical Research Letters*, *48*(6), e2020GL091881. Retrieved from `https://`
870 `agupubs.onlinelibrary.wiley.com/doi/abs/10.1029/2020GL091881`
871 (e2020GL091881 2020GL091881) doi: https://doi.org/10.1029/2020GL091881